



Study of salt migration on the upper part of the Great Wall under the rainfall-radiation cycle

Wenwu Chen^{1,2} · Haoxin Chen^{1,2} · Bobo Jia^{1,2} · Jun Bi³ · Xiang Li^{1,2}

Received: 20 May 2021 / Accepted: 24 August 2022 / Published online: 15 September 2022
© Springer-Verlag GmbH Germany, part of Springer Nature 2022

Abstract

Erosion diseases often appear on the upper part of the Great Wall of China. Low precipitation, intense solar radiation, and severe soil salinization occur in northwest China, and the migration of salt and damage can be described with respect to the rainfall-radiation cycle. Rainfall and radiation conditions were simulated in the laboratory, and reproduced samples were subjected to cyclic experiments to determine salt migration and the damage progress. Surface hardness and ultrasonic velocity were used to measure the surface damage, and the microstructure damage was determined by computed tomography and scanning electronic microscopy. The results show that under the rainfall-radiation cycle, most of the salt in the upper part, including sulfate, migrates to an area 2–3 cm from, while a small part of the salt, including chloride, moves down into the lower half of the sample. In areas where salt is concentrated, the soil density decreases, cracks develop, and a vulnerable zone appears, reducing the surface hardness and ultrasonic velocity. The concentration of salt causing destruction of the soil structure is the main factor leading to erosion of the upper walls of earthen sites. Infiltration of rainwater is required for the migration of soluble sulfate and the damage to soil on the upper wall. Increasing radiation intensity would greatly accelerate the migration of soluble sulfate and damage to the soil structure.

Keywords Earthen sites · Upper erosion · Disease mechanism · Salt migration · Computed tomography

Introduction

Earthen sites use soil as a main building material and represent the oldest and most extensive ancient heritage structures in the world (Li et al. 2011). Earthen sites include the Great Wall of China, ancient cities, historic houses, time-honored tombs, and kiln sites, all of which are valuable to history and culture (Elert et al. 2021). In northwest China, especially along the ancient Silk Road (Li et al. 2010), there are numerous precious earthen sites; the Great Wall is one of the most precious. The Great Wall is a majestic defensive construction project built by the ancient Chinese dynasties, and it is the symbol of the great spirit of China. As early as several hundred years ago, it was listed as one of the Seven Wonders of the Middle Ages. In 1987, the Great Wall was included in the World Cultural Heritage List by the United Nations. However, the Great Wall is in urgent need of protection because it has significant damage from erosion, cracks, gullies, collapse, and peeling, which endangers its stability and integrity (Richards et al. 2020).

During the site survey, it was noticed that a special erosion area (called “upper erosion” hereinafter) often exists

✉ Wenwu Chen
sungp@lzu.edu.cn

Haoxin Chen
chenhx19@lzu.edu.cn

Bobo Jia
jiabb18@lzu.edu.cn

Jun Bi
bijune@hotmail.com

Xiang Li
lixiang19@lzu.edu.cn

¹ Key Laboratory of Mechanics On Disaster and Environment in Western China of Ministry of Education, Lanzhou University, Lanzhou, Gansu 730000, People's Republic of China

² College of Civil Engineering and Mechanics, Lanzhou University, Lanzhou 730000, Gansu, China

³ College of Transportation Science and Engineering, Nanjing Tech University, Nanjing 211816, Jiangsu, China

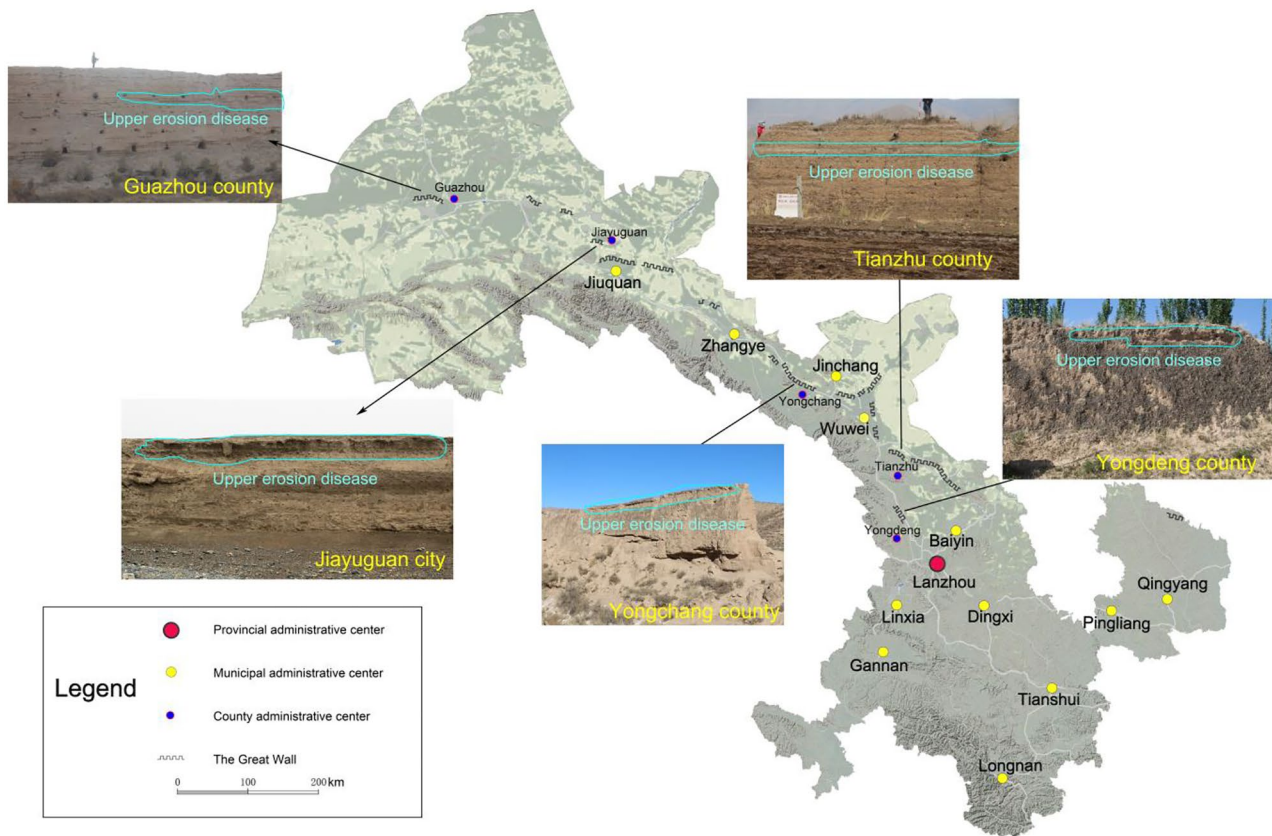


Fig. 1 Photos of upper erosion disease of the Great Wall in Gansu province of China

20–100 cm from the top of the Great Wall. The disease is widespread on the Great Wall located in Jiayuguan City, Yongdeng County, Yongchang County, and many other regions in Gansu Province, as shown in Fig. 1. Past studies have underestimated upper erosion, and it was simply regarded as the abrasion of the wall by sand-carrying wind (Richards et al. 2019). However, there is no any explanation of why the abrasion depth in areas with sand-carrying wind is greater than that of other parts, and there is no explanation for the mechanism of upper erosion. In an investigation of the vertical distribution characteristics of soluble salts on the wall, it was found that the content of soluble salt in the upper erosion area was significantly higher than in other parts. Therefore, the formation of upper erosion may be related to salt migration in the upper wall.

Northwest China is an arid to semi-arid region, with climatic characteristics of low rainfall and strong evaporation; therefore, soil salinization is a serious problem for earthen sites (Wang and Qin 2017). In some areas, the soluble salt content of heritage soil is as high as 5%, which can cause many erosion issues. Research on salt in earthen sites has only recently been launched, but interest in the effects of soluble salt migration on earthen sites is increasing (Mye and Ms 2020). Li et al. (2011) found that the soluble salt

content on the wall surface is higher than in a sample taken from 10 cm inside the wall; under evaporation conditions, the soluble salt content on the upper part of the wall is lower than the soluble salt content on the lower part. Laboratory experiments by Cui et al. (2011) have demonstrated that the accumulation of a large amount of soluble salt at the bottom of the Great Wall is caused by the rise of capillary water at the bottom. Some scholars found that sodium sulfate and sodium chloride were the main migrating salt, and the main cause of disease formation, in soil sites in the northwestern region (Shao et al. 2013). The distribution of sulfate and chloride in lime-based mortars of four soil heritages was discussed by Nogueira et al. (2020). Other studies have also investigated the relationship between salt and heritage building diseases. The change in NaCl concentration during the evaporation process promoted the drying and shrinkage behavior of low plastic soil in an earthen site and caused the surface to crack (Zhang et al. 2017). The geometric patterns in the final crack morphology depended on the NaCl content and layer thickness (Zhang et al. 2016). Mao et al. (2020) found that Na_2SO_4 causes a variety of deformations in heritage buildings, including cracks, collapses, and foundation corrosion. In addition, under freeze–thaw and dry–wet cycle conditions, Na_2SO_4 has greater damage potential than NaCl

(Pu et al. 2016), and Na_2SO_4 is more likely to worsen the mechanical properties and ultrasonic velocity of heritage soil (Shen et al. 2017); therefore, prevention and treatment of salt damage in earthen sites is an urgent problem. Zhang et al. (2020) used the hydrophobicity of polyvinyl alcohol materials to change the direction of salt migration during dry–wet and freeze–thaw cycles in the site soil, which inhibited undercutting. Wheat bran and hemp fiber were used by Wang et al. (2020) as a sacrificial layer to manage cracking and peeling on the surfaces of earthen sites. Cui et al. (2020) used the capillary water blocking effect of the modified cushion to prevent the movement and accumulation of salt from the foundation to the restored area of a heritage site, which prevented the deterioration by salt in the compacted restoration. The research on salt in earthen sites is incomprehensive, and the mechanism of and deterioration by salt migration mostly focuses on the bottom of the structures; therefore, more salt-related research is required on the upper walls of the structures.

In geotechnical engineering, the research on salt migration started earlier and is more systematic. Since Richards (1931) first analyzed water and salt migration in soil considering dynamics and conservation of mass and energy, a large number of experiments and theoretical studies have been conducted on the migration and properties of water and salt in porous media. The survey by Estrelles et al. (2015) showed that the migration and distribution of soil water caused by seasonal rainfall will affect the salt content of regional soil. Drier areas have more serious salinization. Henry et al. (2018) showed that water potential gradient is the main factor affecting salt migration and includes matrix potential, osmotic pressure, and water vapor pressure. Some studies have concluded that the soil temperature range also influenced the evaporation rate and path of water and the distribution of salt. The soluble salts of saline loess more easily migrated to the low-temperature frozen section in experimental studies (Wen et al. 2020). Salt adsorption and heat and mass transfer in the soil affected the migration of salt, as shown by Xu et al. (2020). In conclusion, the main external driving forces for salt migration are temperature and water potential gradients (Zhou et al. 2021). A study on salt migration in the upper walls of earthen sites should also begin with these two factors.

The upper wall of the Great Wall is the part most seriously affected by rainwater infiltration. Rainfall will greatly affect the water potential gradient of the soil and will change the migration of water and salt (Jiang et al. 2016). Because of the climate in northwest China, the Great Wall often is exposed to high-intensity solar radiation after rainfall. Different radiation intensities will affect the soil temperature range and change the temperature gradient. Radiation also accelerates the rate of water evaporation, rapidly changing the water content of each area, affecting the matrix potential

and osmotic potential, and changing the water potential gradient (Helm et al. 2016). Therefore, it is important to study the salt migration laws in the upper wall during the rainfall–radiation cycle. In the field, rainfall and radiation have alternating effects on the Great Wall.

The purpose of this work is to explore the migration laws for various kinds of salts in the upper wall of the Great Wall and explain the mechanism of upper erosion with respect to salt distribution and the rainfall–radiation cycle. Reproduced samples were made from collapsed soil removed from the Great Wall and were subjected to different rainfall and radiation conditions in the laboratory. First, conductivity and ion chromatography were used to clarify the migration law of the salts. Second, photos were taken regularly, the surface hardness and ultrasonic wave velocity were tested, and the failure process of the sample was clarified. Finally, the microstructure of soil samples in the damaged area was observed by computed tomography (CT) and scanning electron microscopy (SEM). The combined results of salt migration and sample damage were used to explain the mechanism of the upper erosion.

Materials and methods

Materials

The study area was located in Yongdeng County, Lanzhou City, Gansu Province, China. This area is located in the northeast of the Qinghai–Tibet Plateau, which is the transitional zone between the Loess Plateau, the eastward extension of the Qilian Mountains, and the Longxi Subsidence basin. The terrain slopes from northwest to southeast, and the altitude is between 1590 and 3650 m. June to September is the most intense period of rainfall and solar radiation; therefore, this period was chosen as the study time. The climatic data (Table 1) show that the heritage buildings in this area were heavily affected by rainfall, sunshine, and wind erosion. The Great Wall in Yongdeng County was established in the Han Dynasty and renovated in the Ming Dynasty under the jurisdiction of Gansu Town. This section of the wall is situated on natural ground and has a length of 1709 m, a residual height of 1.3–4.5 m, a bottom width of 1.2–4.0 m, and a top width of 0.5–2.5 m. It was rammed from local loess, and the rammed layer is 0.18–0.25-m thick.

There are three main reasons for choosing this study site. First, the Great Wall in Yongdeng County is a part of the Ming Great Wall, which was built with the construction technology experience of the Han and Tang Dynasties. It represents China's rammed earth architectural heritage and has very important historical and cultural value. Second, this section of the Great Wall has much erosion damage after hundreds of years of natural weathering, and upper erosion

Table 1 Climatic characteristics of the study area

| Month | Average temperature (°C) | Mean relative humidity (%) | Maximum wind speed (m/s) | Average radiation intensity (W/m ²) | Average daily radiation duration (h) | Average monthly precipitation (mm) | Mean single time rainfall (mm) |
|-------|--------------------------|----------------------------|--------------------------|---|--------------------------------------|------------------------------------|--------------------------------|
| 6 | 15.6 | 61 | 22.3 | 657.4 | 7.69 | 47.9 | 4.6 |
| 7 | 17.6 | 67 | 15.8 | 632.5 | 7.96 | 63.2 | 6.8 |
| 8 | 16.8 | 67 | 17.8 | 584.2 | 7.47 | 67.4 | 6.3 |
| 9 | 12.3 | 71 | 19.4 | 451.2 | 5.71 | 48.1 | 4.2 |
| Mean | 15.6 | 66.5 | 18.8 | 581.3 | 7.21 | 56.6 | 5.5 |

(The data was obtained from the network. <http://data.cma.cn/data/detail/dataCode/J.0012.0004.html>)

is one of the most serious types of erosion. Upper erosion in this area is not continuous, but occurs frequently. One-third of the Ming Great Wall in Yongdeng County has upper erosion, usually occurring at an area 20–100 cm from the top. The erosion is irregular in shape, with a height of 30–100 cm and a depth of 10–30 cm. Finally, the soluble salt content in the soil of the Great Wall in this area varies from 0.1 to 1%, and even can reach 1.5% in some parts. The vertical distribution characteristics of soluble salt on the Ming Great Wall in Yongdeng County are shown in Fig. 2. The ordinate in Fig. 2 shows the distance from the bottom of the wall. The total height of the tested wall was 3 m. The soluble salts in the soil mainly included Na₂SO₄, NaCl, CaSO₄, K₂SO₄, and NaHCO₃. And as shown in Fig. 2, soluble salts were mostly distributed in the bottom and the area 1–2 m from the top. The content of Cl⁻ in the middle and upper parts of the wall is very low, but there is a large amount of Cl⁻ at the bottom. While SO₄²⁻ is distributed at the bottom, it also exists in large quantities at 0.5–1.5 m below the top. The areas where

soluble salts are concentrated are the most damaged parts of the walls.

The soil for the experiment was collected from a collapsed site of the Great Wall in Yongdeng County, Gansu Province, China. The basic properties and soluble salt content of soil are shown in Table 2. This soil was chosen for two reasons: (a) it is a typical soil used in the Great Wall, and (b) it can be obtained without destroying the soil heritage. The soil is very dry and has a relatively high density in its natural state. In addition, the salt content of this soil is high, with Cl⁻ and SO₄²⁻ as the main anions and Ca²⁺ as the main cation Fig. 3 shows the particle size distribution of the test soil. According to *Code for Investigation of Geotechnical Engineering (GB 50021–2001)*, the soil is classified as silty clay.

Methods

Sample preparation

To avoid damage to the Great Wall, artificially reproduced samples were used in this experiment. The preparation process of the soil sample is as follows. After the soil was dried and crushed, it was screened through a 2-mm sieve, and sprayed evenly with distilled water until the moisture content reached 14.5%. (This was the optimum moisture content of the Ming Great Wall in Yongdeng County, as determined in the laboratory). The soil was placed into a

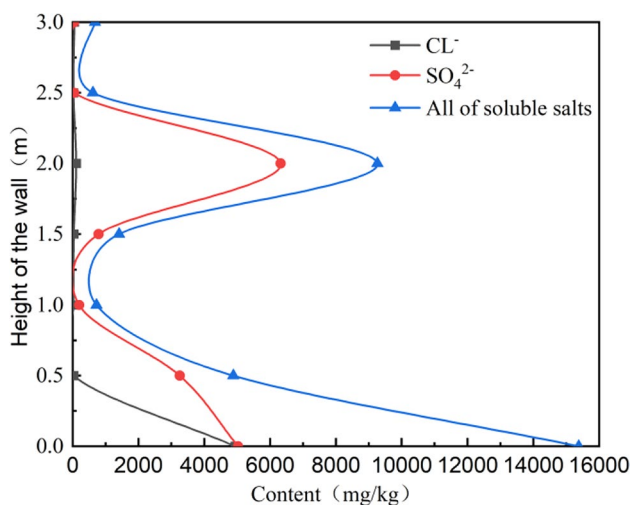


Fig. 2 Vertical distribution characteristics of soluble salt on the Ming Great Wall

Table 2 Properties and ion content of soil

| Soil Properties | Value | Ion species | Content (mg/kg) |
|------------------------------|-------|----------------------------------|-----------------|
| Liquid limit (%) | 26.6 | Cl ⁻ | 438 |
| Plasticity limit (%) | 15.5 | SO ₄ ²⁻ | 550 |
| Plasticity index | 11.1 | Ca ²⁺ | 1810 |
| Specific gravity | 2.67 | Mg ²⁺ | 224 |
| Density (g/cm ³) | 1.59 | Na ⁺ + K ⁺ | 3247 |
| Moisture content(%) | 1.56 | | |

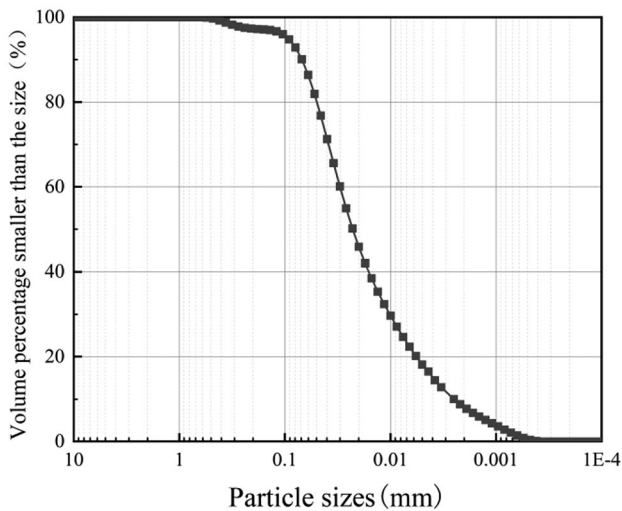


Fig. 3 Grain composition of samples

mold and pressed into a cylindrical sample with a tablet press. The sample diameter was 50 mm and the height was 100 mm. The dry density of rammed earth of the Ming Great Wall in Yongdeng County is 1.61 g/cm³, and previous studies have found that the dry density of the Great Wall in northwest China is generally 1.55–1.75 g/cm³ (Cui et al. 2020). Therefore, the dry density of the reproduced samples in this experiment was set at 1.60 g/cm³. A total of 50 samples were used in the experiment, including 2 blank controls. Each case studied consisted of 12 samples.

After all the soil samples were molded, they were stored in a curing room (temperature, 20 °C; relative humidity, 65%) for 28 d.

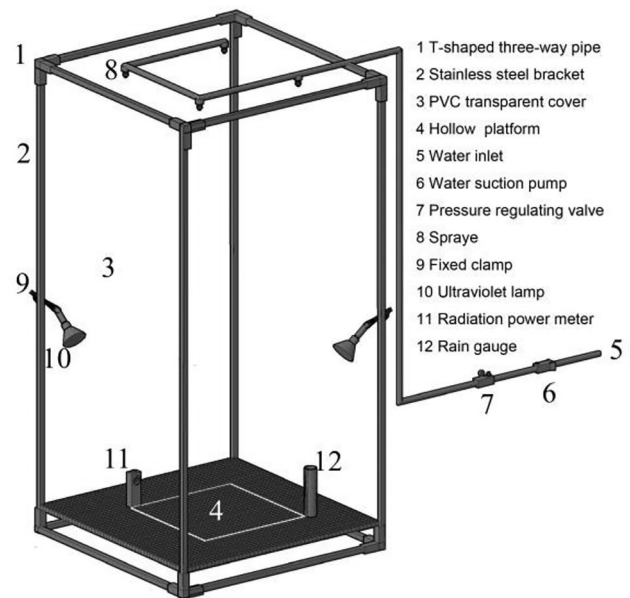


Fig. 5 Rainfall-radiation simulation device

Laboratory cycle tests

Consistent with the climate data in Table 1, laboratory test cases were uniformly established with rainfall of 6 mm, radiation duration of 8 h, high radiation intensity of 700 w/m², and low radiation intensity of 200 w/m². Four types of cycle tests were conducted in this experiment, as shown in Figs. 4 and 5.

In the curing room, the temperature was set to 20 °C and the relative humidity was set to 65%. Deionized water was

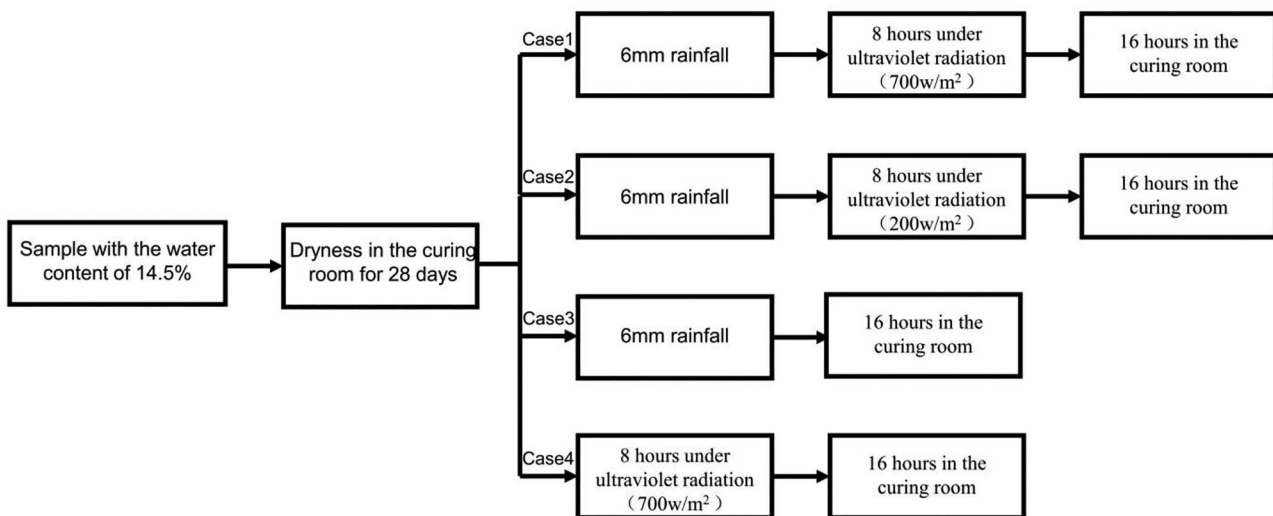


Fig. 4 Rainfall-radiation cycle experiment design

used for the test, and 28 cycles were conducted. Devices to simulate rainfall and solar radiation in the laboratory were used (as shown in Fig. 4). The rainfall simulation device comprised a pump, pressure regulating valve, nozzle, and rain gauge cylinder. The radiation simulation device comprised an ultraviolet lamp and radiation power meter. The devices can be used to adjust rainfall intensity and radiation intensity.

Electrical conductivity test

After 28 cycles, 5 g of soil was taken from 0 cm, 2.5 cm, and 5 cm from the upper surface of the sample. The soil was dried and passed through a 1-mm sieve. The supernatant was mixed with soil to a water-to-soil ratio of 5:1. The electrical conductivity was measured with a REX DDS-307 conductivity meter. Multiple measurements were averaged.

Ion chromatography test

According to the *Standard for Geotechnical Testing Method (GB/T 50123–2019)*, 10 g of soil was collected at 0 cm and 2.5 cm from the upper surface. The soil was dried and ground through a 2-mm sieve. The supernatant was mixed with soil to a water-to-soil ratio of 5:1. The concentrations of Cl^- and SO_4^{2-} were measured by ICS-2500 ion chromatography.

Surface hardness test

Shore A Durometers was used to test the hardness of the soil sample. The test position used was on the side wall, 2–3 cm from the top of the sample. The testing process followed *Verification Regulation of Shore A Durometers (JJG 304–2003)*. The sample surface was measured 10 times, and the readings were averaged to represent the Shore hardness of the sample surface.

Ultrasonic tests

Ultrasonic testing was used to estimate the internal structure of a sample by analyzing the change in ultrasonic velocity through the sample. The primary wave (P-wave) was usually used, which is fast and has little interference in rock and soil mass quality testing (Kahraman and Sciences 2002). Two sensors (a transmitter and receiver) with a frequency of 50 kHz were used in this measurement. An ultrasonic coupler was used to improve the surface contact between the sensor and the test sample to increase the signal-to-noise ratio. The instrument was calibrated with standard materials before each test. Each sample was measured three times, and the average value was taken as the result.

Computed tomography (CT)

CT machines emit X-rays to penetrate the sample and collect data through radiation detectors. A sample will absorb a certain amount of X-rays, and this absorption is observed as attenuation. A sample with greater density will more strongly attenuate the incident X-rays. The relationship between CT value and density ρ is shown in Eq. 1.

$$\rho = \mu_w \left(1 + \frac{H}{1000}\right) / \mu_m \quad (1)$$

where μ_w and μ_m are the X-ray absorption coefficients of water and of a particular substance, respectively, and H is the CT value.

The CT value increases with density. The CT value can evaluate density differences between each part in a more detailed manner compared with the ring knife method and the wax seal method. A Philips Brilliance 16 multi-slice CT scanner was used. The scanning parameters were as follows: layer thickness 1.5 mm; scanning voltage 120 kV; scanning current 185 mA; reconstruction matrix 1024×1024 ; magnification 1; and filter function EC. A RadiAnt DICOM Viewer was used to quickly read the digital imaging and communications in medicine (DICOM) files obtained by CT to obtain the average CT value for each section of the image.

Scanning electronic microscopy

To evaluate the influence on the microstructure of the soil sample after 28 cycles, the sample was tested by Apreo-S SEM and energy-dispersive spectroscopy. The sampling position was located on the side wall, 2–3 cm from the top of the sample. Before the test, the sample was dried and sprayed with gold for 120 s.

Results

Law of salt migration

Migration of all soluble salts

Electrical conductivity increases with ion concentration. Conductivity testing is relatively simple, sensitive, low-cost, and reliable and can be used to characterize the change of soluble salt content in soil (Campbell et al. 1949). Figure 6 shows the variation of the soil sample's electrical conductivity with the number of cycles, revealing the following trends.

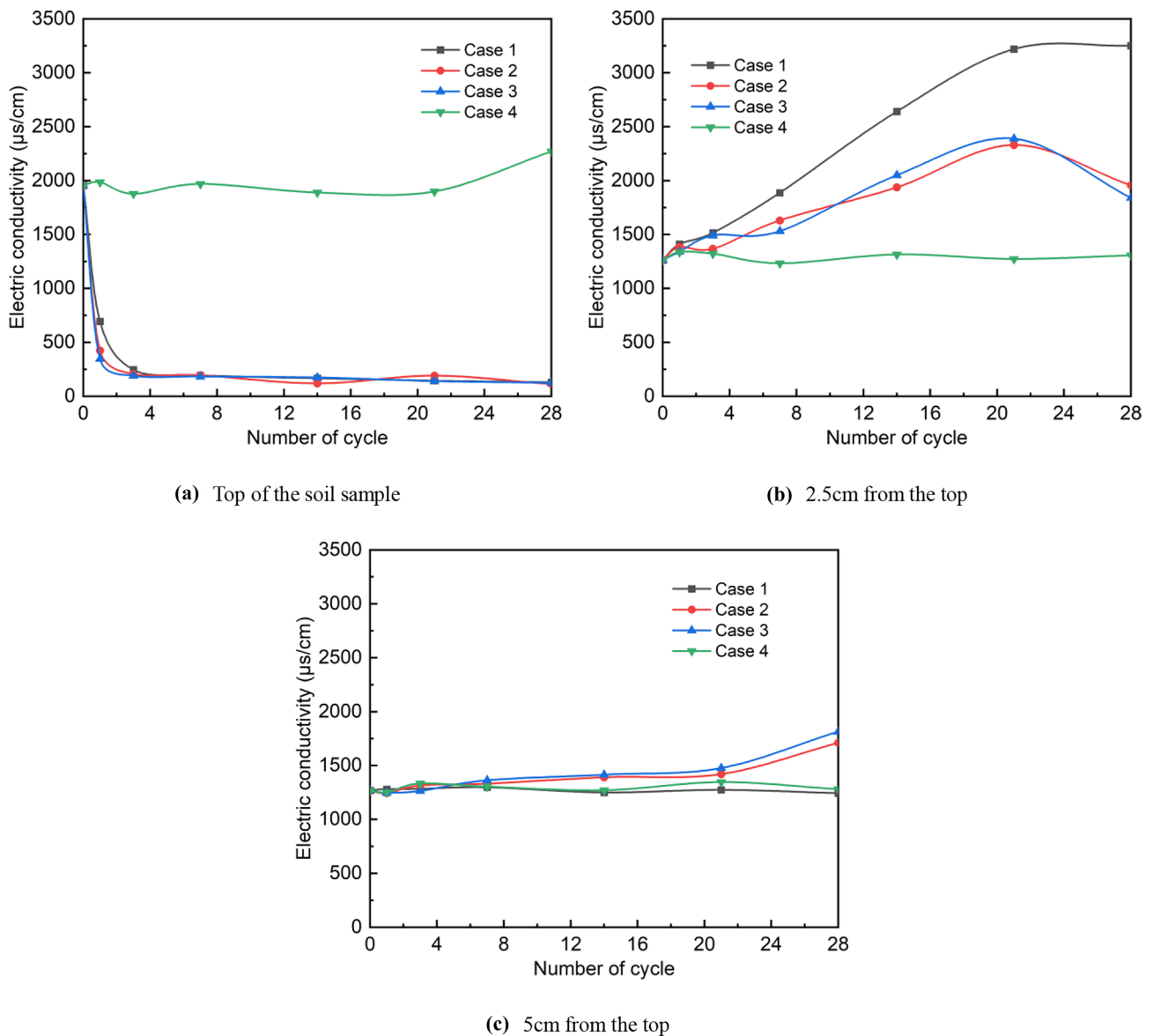


Fig. 6 Graph of conductivity change with number of cycles. **a** Top of the soil sample. **b** 2.5 cm from the top. **c** 5 cm from the top

1. The top of the sample: In cases 1–3, the electrical conductivity dropped sharply and remained stable at approximately 15% of the initial value after 7 cycles. In case 4, the electrical conductivity increased slightly after 14 cycles.
2. 2.5 cm from the top: In case 1, the electrical conductivity gradually increased and reached a stable value after 21 cycles. The stable value was approximately 2.5 times the initial value. In cases 2 and 3, the electrical conductivity increased with the number of cycles until 21 cycles, and then decreased. The electrical conductivity in case 4 was unchanged.
3. 5 cm from the top: The electrical conductivities of cases 1 and 4 were unchanged. Cases 2 and 3 increased significantly

after 21 cycles. The increase was similar to the decrease observed in the samples taken 2.5 cm from the top.

Based on the changes in electrical conductivity in each location, the soluble salt migration law of the sample is as follows: In case 4, the soluble salts in the soil did not significantly migrate. In cases 2 and 3, the soluble salt gradually migrated downward from the top of the sample. After 28 cycles, most of the soluble salts that migrated down were concentrated in an area 2–3 cm from the top, and a small portion of the salts continued to migrate to the lower half of the soil sample. In case 1, the soluble salts that migrated down from the top were concentrated in an area 2–3 cm from

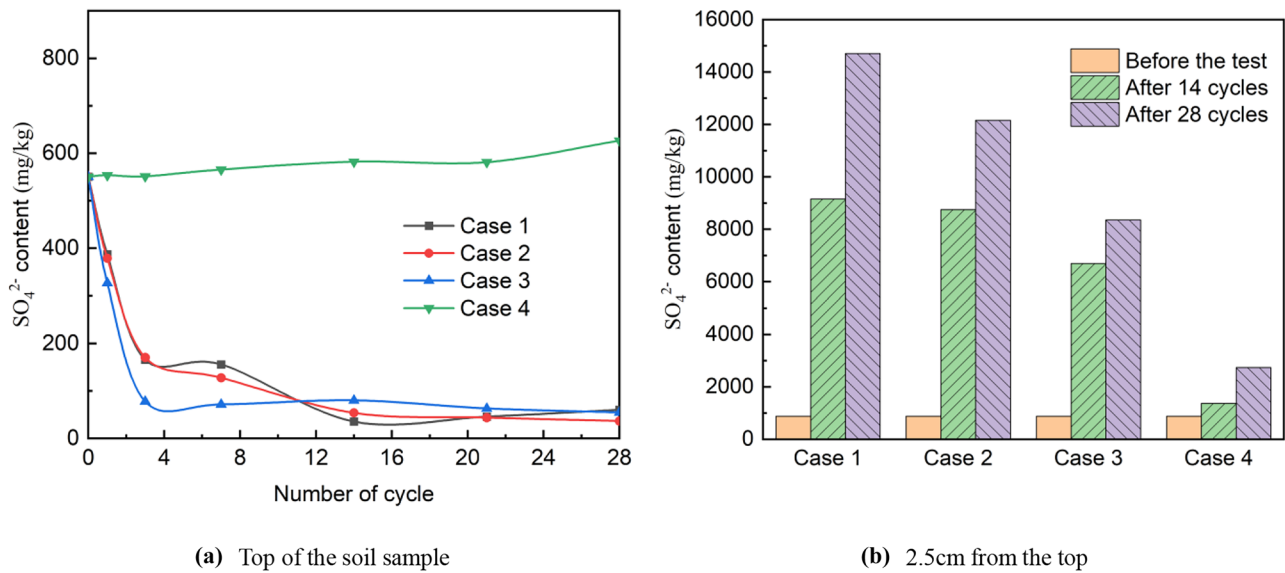


Fig. 7 SO_4^{2-} content change of the sample. **a** Top of the soil sample. **b** 2.5 cm from the top

the top, and the soluble salt concentration in the middle and lower parts remained unchanged.

Sulfate and chloride salts are common soluble salts that affect soil properties, and they exist in large quantities in earthen ruins; therefore, it is necessary to separately analyze the migration laws of Cl^- and SO_4^{2-} .

Migration of SO_4^{2-}

Figure 7 shows how the SO_4^{2-} content of each part of the sample varies with the number of cycles. The migration law of SO_4^{2-} was similar to that of the overall soluble salts. In case 4, the SO_4^{2-} content at the top and 2–3 cm below the sample slightly increased as the test progressed. In the other cases, the SO_4^{2-} content at the top decreased rapidly and stabilized at approximately 10% of the initial value after 14 cycles. As the radiation intensity increased, the rate of decrease slowed. In addition, the concentration of sulfate ion reduced more slowly than the chloride ion in the same conditions. The SO_4^{2-} content increased rapidly in the location 2–3 cm from the top. With increasing radiation intensity, the rate of rise also increases (Germinario and Oguchi 2021). In case 1, the SO_4^{2-} content in the area 2–3 cm from the top reached 1.5% after 28 cycles, which will impact the soil properties.

Migration of Cl^-

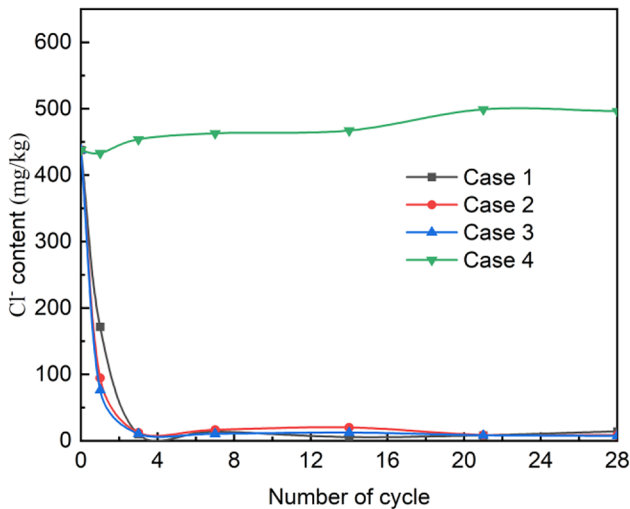
Figure 8 shows how the Cl^- content of each part of the sample varies with the number of cycles. The migration law of Cl^- was different from the migration law of most

soluble salts. For case 4, the Cl^- content at the top of the sample and 2–3 cm below the top slightly increased as the test progressed. In the other cases, the Cl^- content at the top decreased rapidly, reaching a very low value after 7 cycles. The Cl^- content in the area 2–3 cm from the top also decreased rapidly, stabilizing at approximately 10% of the initial value after 28 cycles. The rate of decline decreased as the radiation intensity increased. Cl^- continuously migrated downward from the top through the leaching action of water. Unlike most soluble salts, the Cl^- did not concentrate at 2–3 cm but continued to migrate downward.

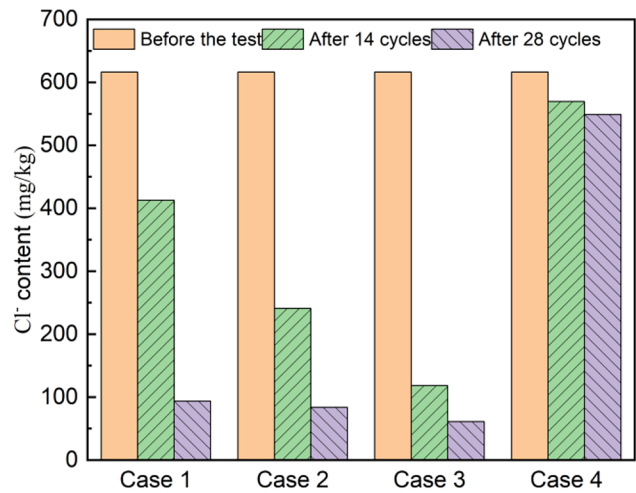
Damage of soil samples

Mass change

By measuring the mass of the soil sample, the change in soil moisture can be used to calculate the evaporation rate. Figure 9a indicates the change in the sample mass during the first cycle. After simulated rainfall, the specimens in cases 1–3 increased in mass by 11 g, which was then evaporated under different cases. In case 1, the mass of the sample first decreased, then increased, then stabilized at the same value as the initial mass. The mass decreased rapidly after 8 h of ultraviolet irradiation. After 6 h, the mass was lower than the initial value, and reached a minimum at 8 h. During 16 h in the curing room, the mass of the samples increased continuously. In cases 2 and 3, the mass of the sample decreased, and reached a stable value after 24 h that was slightly higher than the initial value. In the first 8 h of case 2 and the first



(a) Top of the soil sample



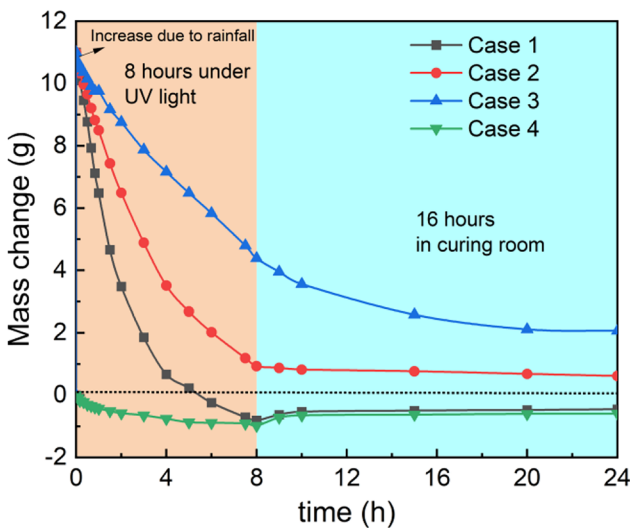
(b) 2.5cm from the top

Fig. 8 Cl⁻ content change of the sample. a Top of the soil sample. b 2.5 cm from the top

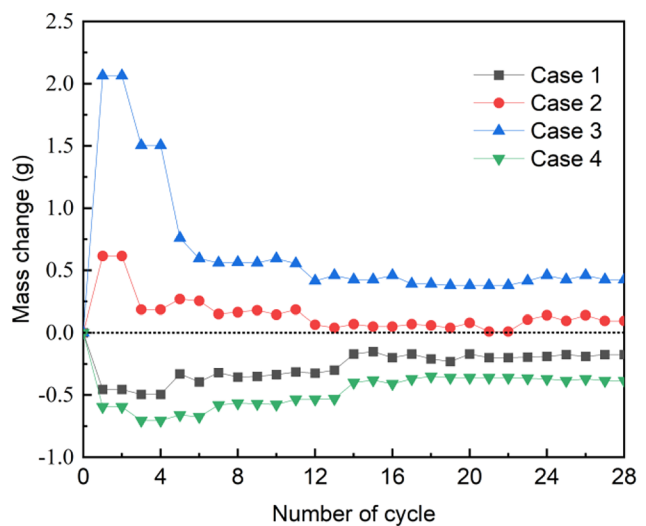
10 h of case 3, the rate of decrease was greater than later in the experiment. For case 4, the mass of the sample slowly decreased during the first 8 h of ultraviolet irradiation. During 16 h in the curing room, the mass of the sample increased gradually, and the final stable value was lower than the initial value.

Figure 9b shows the difference between the mass of the sample and the initial value for each test during the 28 cycles. Cases 2 and 3 had similar changes in mass. In a

single cycle, the 11 g of rainfall infiltration was not completely evaporated; therefore, the mass of the sample significantly increased after the first cycle. During the first seven cycles, the increment between the initial and final mass decreased rapidly and stabilized after 14 cycles; however, it was still higher than the initial value. Cases 1 and 4 also had similar changes in mass. The high-intensity ultraviolet radiation reduced the moisture content of the sample, and the mass of the sample was lower than the original. As the cycle



(a) During the first cycle



(b) During 28 cycles

Fig. 9 Mass change of the soil sample. a During the first cycle. b During 28 cycles

tests progressed, the amount of mass reduction decreased and stabilized after 14 cycles; however, the mass was still slightly smaller than the initial value.

Surface damage

In this study, regular photographs were taken in order to record the surface damage of soil samples during different periods. Figure 10 shows the photographs of samples for the four different cases after 0, 1, 3, 7, 14, 21, and 28 cycles.

In case 1, the soil sample was saturated 2–3 cm from the top after rainfall. Under 700 w/m^2 high-intensity ultraviolet radiation, the water infiltrated and evaporated rapidly. After 3 cycles, the surface of the soil sample appeared to be whitened in the area 2–3 cm from the top. Slight cracks appeared in the whitened area after 14 cycles. At cycle 28, periodic cracks and a vulnerable zone with high salt content (called salty vulnerable zone hereinafter) surrounding the cylindrical soil appeared.

In case 2, the moisture evaporation rate of the sample was less than in case 1. After 3 cycles, the surface of the soil sample appeared slightly whitened in the area 2–3 cm from the top. After 21 cycles, the soil sample began to crack.

After 28 cycles, prominent fissures developed, but no salty vulnerable zone was formed.

After 7 cycles, the surface of the soil sample in case 3 had obvious whitening. After 28 cycles, there were slight cracks in the whitened area but no salty vulnerable zone. The sample in Case 4 did not visibly change.

The damage during the cyclic tests was mainly concentrated in the top 2–3 cm of the sample. In cases 1 to 4, the

damage to the sample gradually increased. Case 4 conditions did not cause visible damage to the sample. The surface of the samples in Cases 1–3 appeared to be whitened and had closed cracks caused by salt enrichment. The surface of the sample in Case 1 had severe typical salt damage including a salty vulnerable zone. The participation of water was an essential condition for the damage, but the increase in radiation intensity also aggravated the destruction of the soil sample.

Surface hardness and ultrasonic tests

Surface hardness is an indicator of resistance of soil to wind erosion, and ultrasonic velocity can be used to evaluate soil quality (Shen et al. 2017). Many studies have shown that higher surface hardness and ultrasonic velocity indicates stronger resistance to wind erosion (Meng et al. 2021). Figures 11 and 12 show the change in surface hardness of the sidewall in the area 2–3 cm from the top and the change in the overall wave velocity of the sample, respectively, with cycle period in the four different cases.

The surface hardness and ultrasonic velocity of samples in Case 4 were basically unchanged. For cases involving rainfall, the surface hardness and overall wave velocity of the side wall in the area 2–3 cm from the top of the sample were significantly reduced. Higher intensity of ultraviolet radiation resulted in a greater reduction. After 28 cycles, the surface hardness was reduced by 23%, and the ultrasonic velocity was reduced by 16%. After the soil sample was exposed to the rain-radiation cycle, the wind erosion resistance of the top 2–3 cm of the soil was reduced, and the internal structure of the soil sample was damaged.

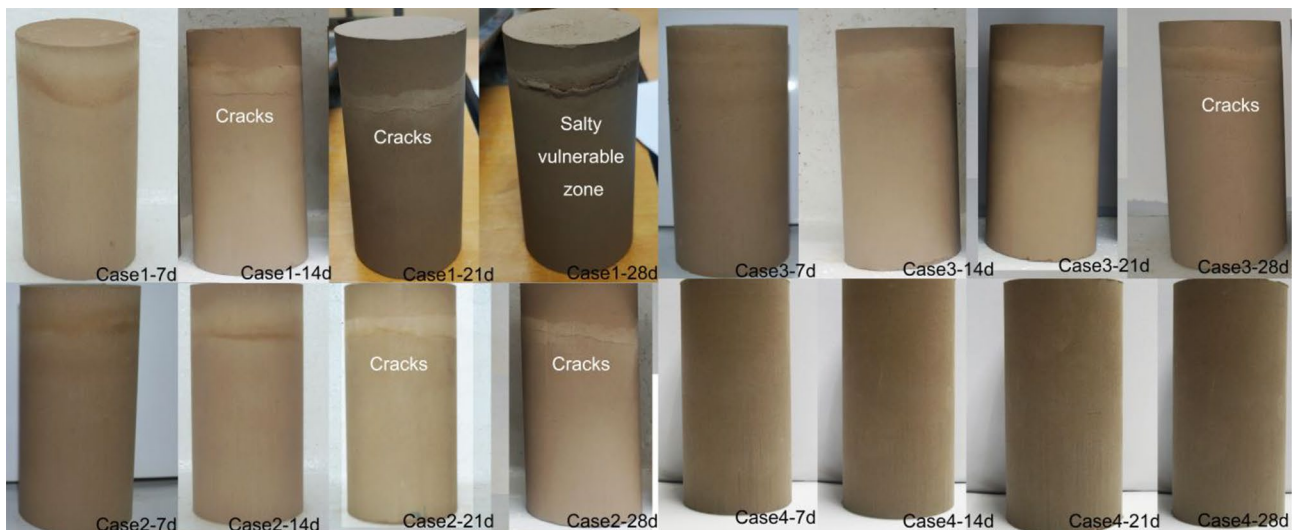


Fig. 10 Surface changes of samples under different cases with cycle period

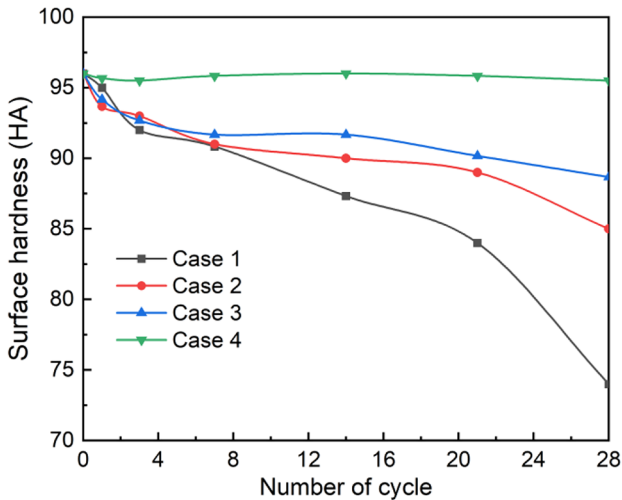


Fig. 11 Average surface hardness varies with cycle period

Microstructural tests

Computed tomography

CT uses precisely collimated X-ray beams, γ -rays, ultrasound, and extremely sensitive detectors to individually scan certain parts of the human body. CT has fast scanning time, provides clear images, and can be used for the inspection of various human diseases. In recent years, researchers have used this technique with geotechnical experiments to study the microstructure, crack development, and density changes of rock and soil without damaging the sample (Fonseca et al. 2019).

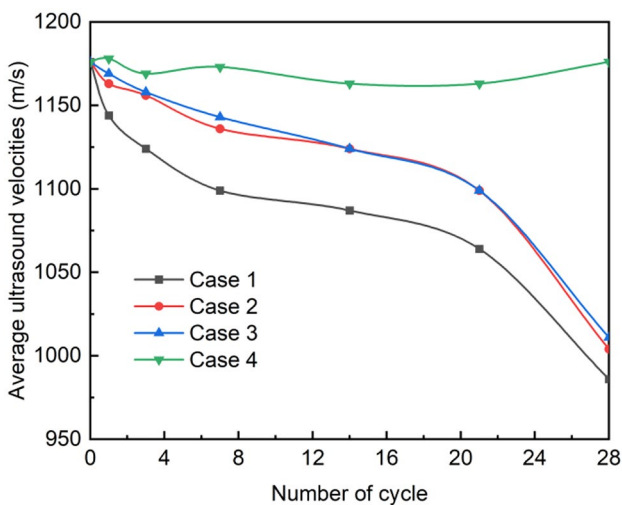


Fig. 12 Average ultrasonic velocity varies with the cycle period

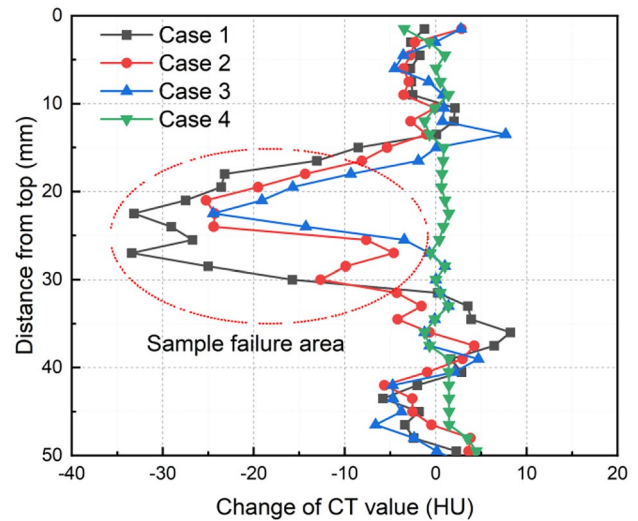


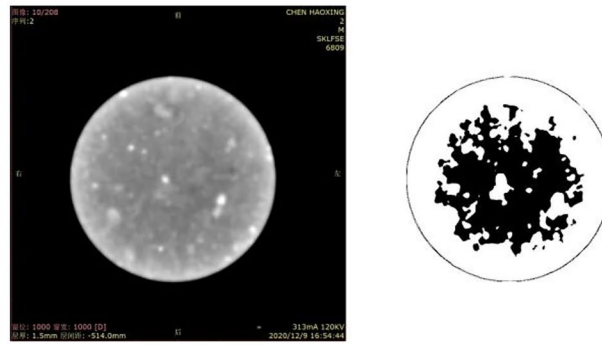
Fig. 13 Change of the average CT value between the state after 28 cycles and the initial

The CT value is extracted from CT images and can reflect the relative density of the material. Figure 13 shows the change in the average CT value of samples after 28 cycles. The change in average CT value for the sample in case 4 and the untested sample almost completely overlapped, indicating that after 28 cycles of ultraviolet radiation, the density of the sample did not substantially change.

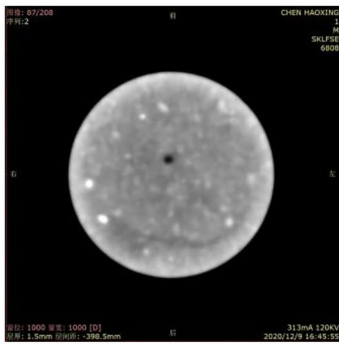
Compared with that of the sample before the test, the average CT value of the area 2–3 cm from the top of the case 1–3 sample was significantly reduced. A maximum decrease occurred under 700 w/m² high-intensity ultraviolet irradiation, and a minimum decrease occurred with 0 w/m² intensity ultraviolet irradiation. Therefore, after the rain-radiation cycle test, the soil 2–3 cm from the top of the sample was damaged and its compaction was reduced, corresponding to the surface failure of the soil sample shown in Fig. 9.

To study the damage to the sample (i.e., the part in the red circle in Fig. 13), Adobe Photoshop CS6 was used to extract the image of this soil area from the CT photograph. The image was imported into PCAS2321 software and the tolerance value was set to 25 for binarization. The left side of Fig. 14 shows the CT photos of the transverse section of the soil sample in the area 2–3 cm from the top for different cases after 28 cycles, and the right side of Fig. 14 shows the picture after binarization. The black area after value processing represents the area with larger gray scale, smaller CT value, and lower soil density. Figure 14a shows the CT images before the test. Because the CT images before the tests for cases 1 to case 4 were similar, only one image was included as a control.

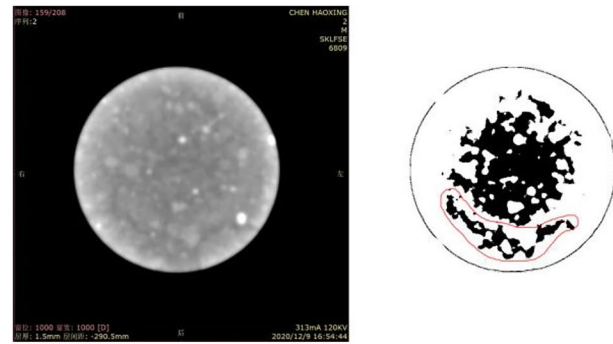
The binarized image from Case 4 was similar to that before the test. However, the binarized images from cases



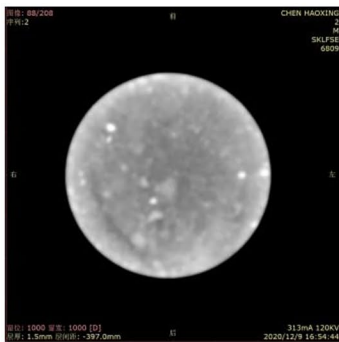
(a) Before the test



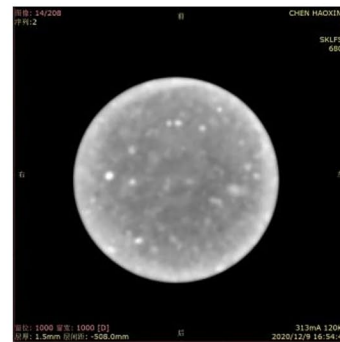
(b) Case 1



(c) Case 2



(d) Case 3



(e) Case 4

Fig. 14 CT photos and binarization images of samples on the area 2–3 cm from the top after 28 cycle. **a** Before the test. **b** Case 1. **c** Case 2. **d** Case 3. **e** Case 4

1–3 have an arc-shaped area (marked by the red circle in Fig. 13) near the edge of the circular section. This area indicates that the soil at the edge of the cross-section was damaged during the test, forming the arc-shaped area with lower density. Table 3 contains the statistics for the area ratio, major axis length, mean CT value, and minimum CT value from the black graphics in the arc-shaped area. From case 1 to case 3, the proportion of black area in the red circle gradually decreased, the length decreased, and the average

Table 3 CT data in red circle

| Type | Area ratio | Major axis length (mm) | Mean CT value (HU) | Minimum CT value (HU) |
|--------|------------|------------------------|--------------------|-----------------------|
| Case 1 | 4.76% | 35.4 | 966.4 | 943 |
| Case 2 | 4.48% | 32.4 | 1011.4 | 978 |
| Case 3 | 1.42% | 21.9 | 1011.6 | 984 |

and minimum CT values gradually increased. Therefore, as the radiation intensity increased, soil damage in this area also increased. The position of fissure development was similar in the damage zone and the soil sample.

Scanning electron microscopy

The microstructure of the soil is based on qualitative analysis, which shows the unit bodies and pores of the soil. Figure 15 shows the SEM photos of the soil surface in the area 2–3 cm from the top after 28 cycles. The magnification of all SEM photos is $500\times$. The untested soil samples have more cementitious materials, no single unit body can be distinguished, and the soil particles have few rock-forming debris. The basic unit body constituting the surface is a sheet-like aggregate, and the surface morphology is relatively flat. After the rainfall-radiation cycle, the pores and structure of the soil have significantly changed. There is less cementation material between the soil particles, and the flake-like aggregates are split into many aggregates of 10–80- μm diameter and some fine particles of $<10\ \mu\text{m}$ diameter. There are many edge-to-surface contacts and edge-to-edge contacts between particles, making the connections looser than they used were previously. The pores between the particles significantly increased, and large pores spanning several units appeared. The surface morphology was no longer flat, and some soil particles are slightly upward. In case 4, the microstructure of the soil did not significantly change during the test, but some holes did appear between the particles.

Discussion

Law of salt migration

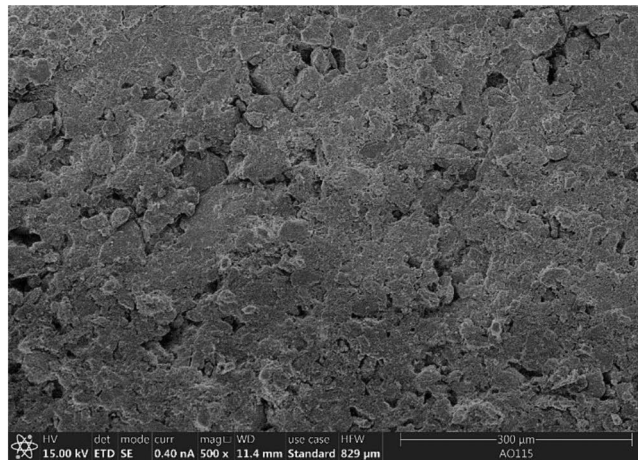
Electrical conductivity measurements show that the salinity in the soil did not significantly migrate, but only slightly increased on the upper surface under the conditions of radiation but no rainfall. Wen et al. (2020) concluded that the salt migration in soil under the influence of a temperature gradient was very small under dry conditions. The water in the soil pores is the most dynamic component of the soil, and the most important transport carrier for soluble salts. In this experiment, in the absence of rainfall, the soil samples were always in a state of low moisture content (below 1%). There was virtually no water migration through the soil, and the soluble salt content and composition in the sample did not significantly change under sunlight. The salt content on the upper surface increased because a small amount of water on the upper surface evaporated upwards and entrained a small amount of soluble salt.

In contrast, a large amount of soil salinity migrated downward from the top under simulated rainfall. Most soluble salt

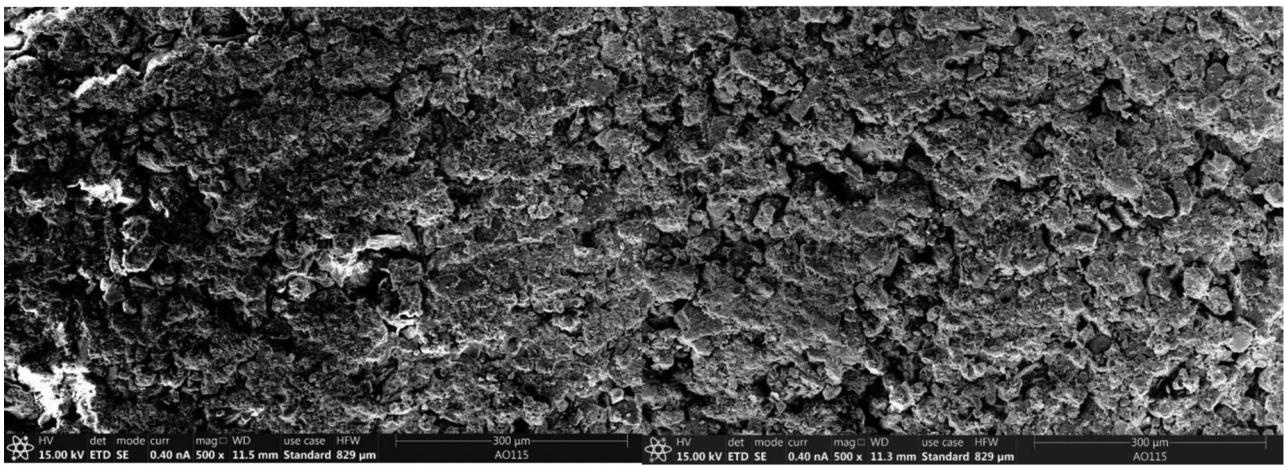
ions, including SO_4^{2-} , are concentrated in the area 2–3 cm from the top of the sample, while Cl^- continues to move downward to the lower half of the soil sample. The enhanced intensity of the simulated radiation increases the soluble salt content concentration in the area 2–3 cm below the surface. This process explains the vertical distribution of salt in the wall of the Ming Great Wall, which has an area with concentrated salt close to the top of the wall.

The concentration of salt in the area 2–3 cm from the top may be because of the balance between water penetration under gravity and evaporation under radiation. After 6 mm of rainfall, the top of the sample was infiltrated by water to a depth of 2 cm, and the water was constantly evaporating while infiltrating. The intensity of radiation affects water evaporation (Mahmood and Hubbard 2005). Under high-intensity ultraviolet radiation, the water evaporation rate is extremely high. When evaporation was greater than the upward soil moisture flux, a dry surface layer was formed (Agam 2004), increasing the upward flow of soil moisture and reducing the distance of rainfall infiltration. Therefore, the moisture only penetrated down approximately 1 cm before it was completely evaporated, and only a small amount of water quickly penetrated along the soil pores and micro-cracks. Many studies have shown that the distance of salt migration depends on the distance of water infiltration; therefore, it is reasonable that most salt is carried from the top to approximately 2–3-cm depth by water leaching. As radiation intensity decreased, the evaporation rate decreased and more water infiltrated. More ions, including SO_4^{2-} , migrated downward, and the soluble salt content in the area 2–3 cm from the top was lower than in the high-intensity radiation cases.

The observation that Cl^- migrates downward while SO_4^{2-} accumulates closer to the surface after rainfall stops infiltrating is worthy of discussion. Cui et al. (2011) found that a large amount of soluble salt, including NaCl, accumulated at the bottom of many earthen sites, while the Na_2SO_4 content was lower because of rising capillary water from the bottom. The impact of rainwater infiltration from the top and the rising of capillary water from the bottom have opposite effects, but the inherent laws are the same. Different ions may have different migration speed because of their adsorption and diffusion characteristics in porous media, resulting in the observed ion differentiation (Bresler and Management 1981; Kemper and Schaik 1966). In general, Cl^- and SO_4^{2-} undergo non-specific adsorption (also known as physical adsorption), where ions are absorbed on the outer layer of the diffusion double layer through the combined actions of electrostatic attraction of the soil surface charge and thermal movement of ions. The non-specific adsorption force is related to the number of charged ions. SO_4^{2-} has a higher charge and is more strongly adsorbed by soil particles and migrates more slowly; therefore, it stagnates in the area

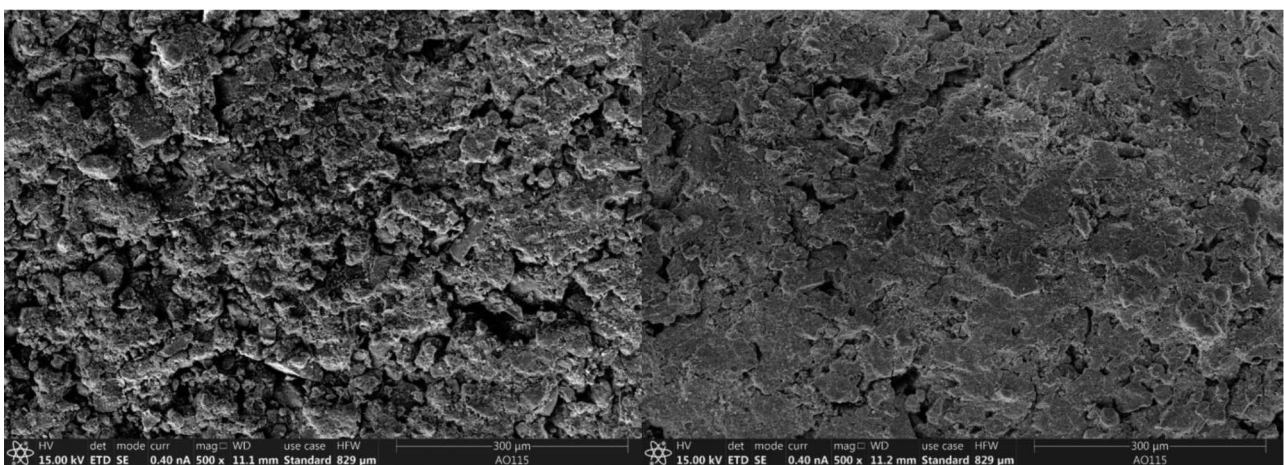


(a) Before the test



(b) Case 1

(c) Case 2



(d) Case 3

(e) Case 4

Fig. 15 SEM photos of soil surface on the area 2-3 cm from the top after 28 cycles. **a** Before the test. **b** Case 1. **c** Case 2. **d** Case 3. **e** Case 4

2–3 cm from the top. The adsorptive force of the soil particles on Cl^- is weaker, and the diffusion rate is very rapid through the soil pores. A small amount of infiltrating water can also migrate with Cl^- . In capillary water rising from the bottom, the adsorption force of Cl^- is lower than that of SO_4^{2-} ; therefore, more Cl^- is carried by capillary water to the bottom of the Great Wall and becomes the main soluble salt. Cl^- and SO_4^{2-} have different distributions and ion differentiation is the likely cause of the salt distribution differences in earthen heritage.

Cause of specimen failure

The surface hardness tests, ultrasonic velocity tests, and microstructure photos show that the soil samples are not damaged under radiation with no rainfall. Case 4 represents a high-low temperature cycle. Under 700 w/m^2 high-intensity ultraviolet radiation, the soil surface heats up rapidly, and the soil interior heats up slowly. After irradiation, the soil sample cools down until it reaches the curing room temperature. Thermal expansion and contraction of soil particles continuously impacts the original structure of soil particles, and this repeated action causes soil damage (Ahmadi et al. 2021). However, the damage occurs over a long time, with no obvious effect after only 28 cycles. Therefore, there was no obvious damage observed on the surface of the sample in Case 4, and the soil microstructure of the sample did not change.

In contrast, the damage of the sample was concentrated in the area 2–3 cm from the top under simulated rainfall. This is where sulfates are concentrated, and higher sunlight intensity results in higher sulfate concentration and more serious damage. The destruction process occurs where high salinity leads to whitening and discoloration, cracks develop, and expand, and the salty vulnerable zone is formed through the cracked area. Simultaneously, the surface hardness and the ultrasonic velocity of the sample decrease, and the ability to resist wind erosion is reduced.

The damage to the sample is caused by the changing dry and wet state of sulfate-containing soil during the rain-radiation cycle. Many studies have shown that long-term dry–wet cycles weaken the physical and mechanical properties of soil (Albrecht and Benson 2001; Chen and Ng 2013). Tang et al. (2020) studied the influence of dry–wet cycles on unsaturated soils and found that the density of unsaturated soils decreases and more cracks develop with an increasing number of dry–wet cycles; this process explains the decreased CT value and the development of cracks in the area 2–3 cm from the top of the sample.

In addition, in engineering practice, soil with a sulfate content of more than 0.3% is called sulfate saline soil. As early as 1960, it was recognized that soils containing high concentrations of water-soluble sulfates exhibited a swelling phenomenon similar to swelling clay. Peng et al. (2019)

proved that sodium sulfate and water vapor would combine to form sodium sulfate decahydrate during the evaporation process, causing the salt to expand in volume. Li et al. (2011) found in the investigation that due to the crystallization of salt, the volume change after dissolution, and the repeated effects of expansion and contraction, the soil structure was constantly loosened, and the vulnerable zone was formed on the surface of the soil heritage finally. Therefore, the sulfate salt concentrated on area 2–3 cm from the top of the sample was dissolved by the infiltration of rainwater, and then the sulfate crystals were precipitated quickly during the rapid evaporation of water. The swelling effect of sulfate expanded the pores and gradually loosens the soil structure, which eventually led to the formation of the salty vulnerable zone.

Development mechanism of upper erosion

Combining the law of salt migration from this experiment and the location of sample damage provides a preliminary explanation of how erosion occurs on the upper part of the Great Wall. Figure 16 shows the five steps of the formation of upper erosion: The Great Wall suffers from rainfall infiltration and rapid evaporation under solar radiation, which causes the salts in the wall to migrate, concentrating sulfate in the area near the top of the wall (inferred from laboratory tests and field surveys). With the continuous destruction of the soil by sulfate, the compaction decreases, and cracks gradually develop in local areas. As the salt content increases, the deterioration in the soil steadily intensifies, and the surface soil becomes fragile and forms a salty vulnerable zone. The resistance of the wall surface to wind erosion is greatly reduced by the formation of cracks and the salty vulnerable zone.

Northwest China is windy, and the strong winds often entrain sand, which has a serious erosion effect on earthen sites (Zhang et al. 2010). Compared with those on other parts of the wall, surface peeling and abrasions in this area are more severe, forming an eroding zone. These five steps occur in a continuous loop. Under the gradual damage occurring over the years, the depth of erosion in this zone has been more extensive than on other parts of the Great Wall, resulting in macroscopically visible upper erosion.

The laboratory test cases are not exactly the same as the actual engineering cases of the Great Wall in the field. In the laboratory, the location of salt concentration and destruction was 2–3 cm from the top in the experiment, while in the field it was 20–100 cm from the top of the earthen sites. This may be because the intensity of rainfall and radiation conditions in the laboratory are stable, unlike the complex and changeable climate conditions in the field. During heavy rainfall or when water accumulates on the top of the wall, the depth of rainwater infiltration will be much greater than observed in the laboratory. In addition, when radiation intensity is low,

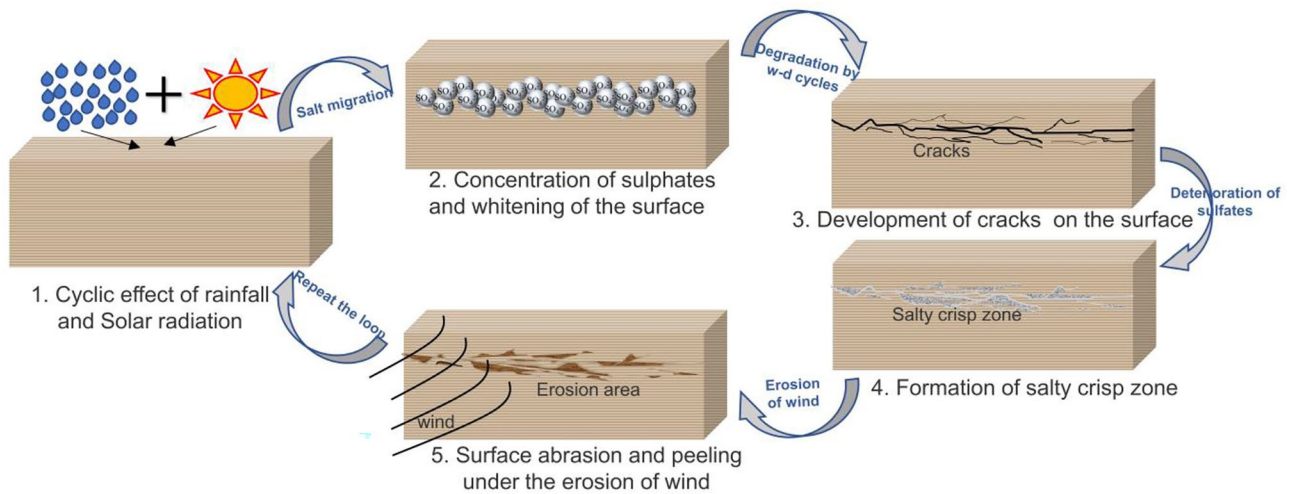


Fig. 16 Upper erosion disease development process of the Great Wall

the evaporation rate of rainwater slows down and the infiltration distance increases, causing the salt in the upper part of the earthen ruins to migrate longer distances.

To demonstrate this, the distance from the top of the Ming Great Wall in eight regions of Gansu province was measured and analyzed with the local rainfall and radiation intensity. As shown in Figs. 17 and 18, the distance is positively correlated with rainfall and negatively correlated with radiation intensity, which supports this hypothesis.

For Fig. 17, more rainfall causes rainwater to infiltrate and salt to migrate farther, which make erosion disease move further from the top of the wall. For Fig. 18, the result is consistent with the experimental photos shown in Fig. 10.

Greater solar radiation intensity will increase the evaporation rate of rainwater and reduce the migration distance of salt, thereby affecting the location of erosion. The R^2 is only 0.583, which makes the negative correlation implausible. There may be two reasons for it. First, only 8 samples were used for the analysis. Because the number of samples is not enough, there is a little deviation in the fitting results. On the other hand, the relationship between radiation intensity and the development position of erosion disease may be uncertain under the interference of other environmental factors. Wind, temperature and other environmental conditions may also be involved in the formation of erosion disease.

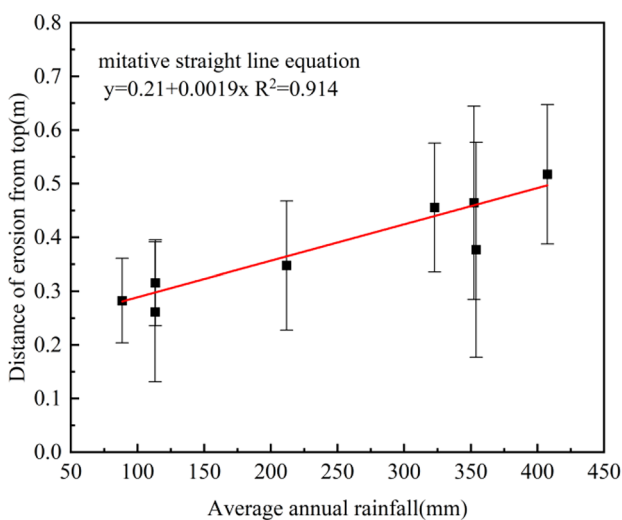


Fig. 17 The relationship between rainfall and distance of erosion from top

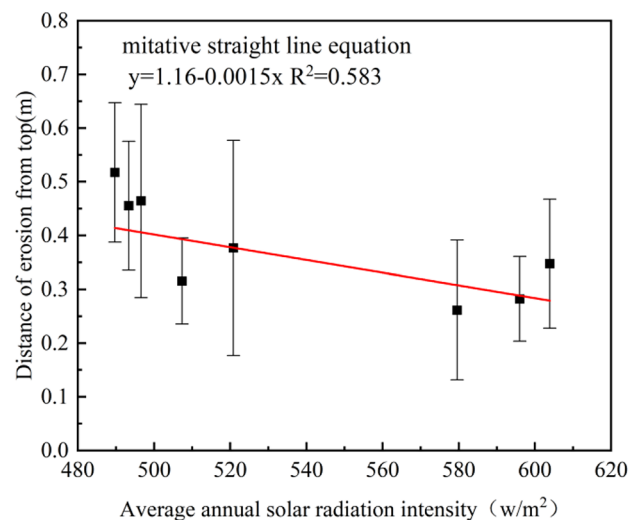


Fig. 18 The relationship between solar radiation intensity and distance of erosion from top

However, the depth and width of the erosion observed in the laboratory are different from what is observed on the Great Wall, possibly because the laboratory tests only lasted 28 cycles, and their effects resulted in less damage than has occurred on the soil ruins over hundreds of years.

Nevertheless, this experiment indicates that erosion on the upper part of the Great Wall is closely related to salt migration and damage caused by the rainfall-radiation cycle. This pilot research explains the erosion on the upper part of the Great Wall with respect to salt migration and provides a reference for the development of a mechanism for soil heritage diseases.

Conclusion

To study the influence of the rainfall-radiation cycle on salt migration on the upper walls of earthen sites in northwest China and the mechanism for the development of upper erosion, tests were carried out to simulate the rainfall-radiation cycle. Based on these tests, the conclusions are as follows:

1. Under rainfall conditions, most soluble salt ions, including SO_4^{2-} , were concentrated in the area 2–3 cm from the top of the sample, while Cl^- moved down to the lower half of the soil sample. Simulated radiation intensity increased the concentration of soluble salts in this area. The balance between infiltration of rainwater by gravity and the evaporation by radiation, and the difference in the migration speed caused by different adsorption and diffusion characteristics, may be the reasons for this law.
2. The soil samples were not damaged in the short time they were exposed to radiation with no rainfall. Under rainfall conditions, the damage of the sample was mainly focused in the area where sulfate was concentrated. The effect of sulfate on the soil during the dry–wet cycle reduces the soil compaction in this area, developing and expanding cracks, and forming a salty vulnerable zone through the cracks.
3. The development of erosion diseases on the upper part of the Great Wall is closely related to the migration of salt under the rainfall-radiation cycle. The destruction by high concentrations of salt will worsen the soil properties on the upper part of the wall compared with other parts, such that these areas are more easily worn and peeled by wind, forming upper erosion disease over time. The increase in radiation intensity will accelerate the development of erosion diseases.

Acknowledgements Special thanks to Haiyu Wu and Yilun Qin for her valuable help in the experiments.

We thank Tara Penner, MSc, from Liwen Bianji (Edanz) (www.liwenbianji.cn/), for editing the English text of a draft of this manuscript.

Funding This work was supported by the National Key R&D Program of China. No.2020YFC1522201.

Declarations

Conflict of interest The authors declare no competing interests.

References

- Agam N (2004) Soil water evaporation during the dry season in an arid zone. *J Geophys Res* 109:103. <https://doi.org/10.1029/2004jd004802>
- Ahmadi S, Ghasemzadeh H, Changizi F (2021) Effects of thermal cycles on microstructural and functional properties of nano treated clayey soil. *Eng Geol* 280:105929. <https://doi.org/10.1016/j.enggeo.2020.105929>
- Albrecht BA, Benson CH (2001) Effect of Desiccation on Compacted Natural Clays. *J Geotech Geoenviron Eng* 128:67–75. [https://doi.org/10.1061/\(ASCE\)1090-0241\(2001\)127:1\(67\)](https://doi.org/10.1061/(ASCE)1090-0241(2001)127:1(67))
- Bresler E, Management (1981) Transport of salts in soils and subsoils. *Agric Water Manag* 4:35–62. [https://doi.org/10.1016/0378-3774\(81\)90043-3](https://doi.org/10.1016/0378-3774(81)90043-3)
- Campbell RB, Bower C, Richards L (1949) Change of electrical conductivity with temperature and the relation of osmotic pressure to electrical conductivity and ion concentration for soil extracts I. *Soil Sci Soc Am J* 13:66–69. <https://doi.org/10.2136/sssaj1949.036159950013000C0010x>
- Chen R, Ng CW (2013) Impact of wetting–drying cycles on hydro-mechanical behavior of an unsaturated compacted clay. *Appl Clay Sci* 86:38–46. <https://doi.org/10.1016/j.clay.2013.09.018>
- Cui K, Chen WW, Han L, Wang XD, Han WF (2011) Effects of salinized deterioration and aeolian ullage on soils in undercutting area of earthen ruins in arid region. *Chinese J Geotech Eng* 33:1412–1418. <https://doi.org/10.1111/j.1759-6831.2010.00113.x>
- Cui K, Wang D, An X, Yu L, Wu G (2020) Barrier effect of modified cushion on salinity deterioration in the basal sapping zone of earthen sites. *Soil Mech Found Eng* 57:227–236. <https://doi.org/10.1007/s11204-020-09659-y>
- Elert K, García Baños E, Ibañez Velasco A, Bel-Anzué P (2021) Traditional roofing with sandstone slabs: Implications for the safeguarding of vernacular architecture. *J Build Eng* 33. <https://doi.org/10.1016/j.jobe.2020.101857>
- Estrelles E, Biondi E, Galìè M, Mainardi F, Hurtado A, Soriano P (2015) Aridity level, rainfall pattern and soil features as key factors in germination strategies in salt-affected plant communities. *J Arid Environ* 117:1–9. <https://doi.org/10.1016/j.jaridenv.2015.02.005>
- Fonseca ACG, Costa LF, Dantas CC, Heck RJ, Melo SB, Antonino ACD, Barbosa ES (2019) Precise determination of soil structure parameters in a X-ray and γ -ray CT combination methodology. *Prog Nucl Energy* 114:138–144. <https://doi.org/10.1016/j.pnucene.2019.02.007>
- Germinario L, Oguchi CT (2021) Underground salt weathering of heritage stone: lithological and environmental constraints on the formation of sulfate efflorescences and crusts. *J Cult Herit*. <https://doi.org/10.1016/j.culher.2021.02.011>
- Helm P, Stirling R, Glendinning S (2016) The implications of using estimated solar radiation on the derivation of potential evapotranspiration and soil moisture deficit within an embankment. *Procedia Eng* 143:697–707. <https://doi.org/10.1016/j.proeng.2016.06.105>

- Henry CJ, Brant JA, Kelleners TJ (2018) Water transport mechanisms for salt-rejecting membranes driven by soil-water potentials. *J Membr Sci* 563:107–114. <https://doi.org/10.1016/j.memsci.2018.05.041>
- Jiang Z, Li X, Wu H, Xiao X, Chen H, Wei J (2016) Using electromagnetic induction method to reveal dynamics of soil water and salt during continual rainfall events. *Biosys Eng* 152:3–13. <https://doi.org/10.1016/j.biosystemseng.2016.03.011>
- Kahraman S, Sciences A (2002) Estimating the direct P-wave velocity value of intact rock from indirect laboratory measurements. *Int J Rock Mech Min Sci* 39:101–104. [https://doi.org/10.1016/S1365-1609\(02\)00005-9](https://doi.org/10.1016/S1365-1609(02)00005-9)
- Kemper WD, Schaik J (1966) Diffusion of salts in clay-water systems I. *Soil Sci Soc Am J* 30:534–540. <https://doi.org/10.2136/sssaj1966.036159950030000500006x>
- Li L, Shao M, Wang S, Li Z (2010) Preservation of earthen heritage sites on the Silk Road, northwest China from the impact of the environment. *Environ Earth Sci* 64:1625–1639. <https://doi.org/10.1007/s12665-010-0829-3>
- Li Z, Wang X, Sun M, Chen W, Guo Q, Zhang H (2011) Conservation of Jiaohe ancient earthen site in China. *J Rock Mech Geotech Eng* 3:270–281. <https://doi.org/10.3724/sp.J.1235.2011.00270>
- Mahmood R, Hubbard KG (2005) Assessing bias in evapotranspiration and soil moisture estimates due to the use of modeled solar radiation and dew point temperature data. *Agric For Meteorol* 130:71–84. <https://doi.org/10.1016/j.agrformet.2005.02.004>
- Mao W, Shen Y, Zhu Y, Bai Y, Sun M (2020) Disentangling the deformation process of earthen sites and understanding the role of Na₂SO₄ and precipitation: a case study on the Great Wall Relics of the Ming Dynasty in Yulin, China. *Stud Conserv* 66:51–63. <https://doi.org/10.1080/00393630.2020.1751976>
- Meng H, Gao Y, He J, Qi Y, Hang L (2021) Microbially induced carbonate precipitation for wind erosion control of desert soil: Field-scale tests. *Geoderma* 383:114723. <https://doi.org/10.1016/j.geoderma.2020.114723>
- Mye A, Ms B (2020) An assessment of capillary water absorption changes related to the different salt solutions and their concentrations ratios in the Der tuff (Afyonkarahisar-Turkey) used as building stone of cultural heritages. *J Build Eng* 35:102102. <https://doi.org/10.1016/j.jobe.2020.102102>
- Nogueira R, Ferreira Pinto AP, Gomes A (2020) Artificial ageing by salt crystallization: test protocol and salt distribution patterns in lime-based rendering mortars. *J Cult Herit* 45:180–192. <https://doi.org/10.1016/j.culher.2020.01.013>
- Peng S, Wang F, Fan L (2019) Experimental study on influence of vaporous water on salt expansion of sulfate saline soil. *Adv Civil Eng* 2019:1–9. <https://doi.org/10.1155/2019/6819460>
- Pu T, Chen W, Du Y, Li W, Su N (2016) Snowfall-related deterioration behavior of the Ming Great Wall in the eastern Qinghai-Tibet Plateau. *Nat Hazards* 84:1539–1550. <https://doi.org/10.1007/s11069-016-2497-4>
- Richards J, Viles H, Guo Q (2020) The importance of wind as a driver of earthen heritage deterioration in dryland environments. *Geomorphology* 369:107363. <https://doi.org/10.1016/j.geomorph.2020.107363>
- Richards J, Zhao G, Zhang H, Viles H (2019) A controlled field experiment to investigate the deterioration of earthen heritage by wind and rain. *Herit Sci* 7:51. <https://doi.org/10.1186/s40494-019-0293-7>
- Richards LA (1931) Capillary conduction of liquids through porous mediums. *Physics* 1:318–333. <https://doi.org/10.1063/1.1745010>
- Shao M, Li L, Wang S, Wang E, Li Z (2013) Deterioration mechanisms of building materials of Jiaohe ruins in China. *J Cult Herit* 14:38–44. <https://doi.org/10.1016/j.culher.2012.03.006>
- Shen Y-X, Chen W-W, Kuang J, Du W-F (2017) Effect of salts on earthen materials deterioration after humidity cycling. *J Central South Univ* 24:796–806. <https://doi.org/10.1007/s11771-017-3482-0>
- Tang C-S, Cheng Q, Leng T, Shi B, Zeng H, Inyang HI (2020) Effects of wetting-drying cycles and desiccation cracks on mechanical behavior of an unsaturated soil. *CATENA* 194:104721. <https://doi.org/10.1016/j.catena.2020.104721>
- Wang X-D, Zhang B, Pei Q-Q, Guo Q-L, Chen W-W, Li F-J (2020) Experimental studies on sacrificial layer in conservation of earthen sites. *J Cult Herit* 41:74–83. <https://doi.org/10.1016/j.culher.2019.07.003>
- Wang Y-J, Qin D-H (2017) Influence of climate change and human activity on water resources in arid region of Northwest China: An overview. *Adv Clim Chang Res* 8:268–278. <https://doi.org/10.1016/j.accre.2017.08.004>
- Wen W, Lai Y, You Z (2020) Numerical modeling of water–heat–vapor–salt transport in unsaturated soil under evaporation. *Int J Heat Mass Transf* 159:120114. <https://doi.org/10.1016/j.ijheatmasstransfer.2020.120114>
- Xu J, Lan W, Li Y, Wang S, Cheng W-C, Yao X (2020) Heat, water and solute transfer in saline loess under uniaxial freezing condition. *Comput Geotech* 118:103319. <https://doi.org/10.1016/j.compgeo.2019.103319>
- Zhang Q, Chen W, Fan W (2020) Protecting earthen sites by soil hydrophobicity under freeze–thaw and dry–wet cycles. *Constr Build Mater* 262:120089. <https://doi.org/10.1016/j.conbuildmat.2020.120089>
- Zhang Y, Ye W, Chen Y, Chen B (2017) Impact of NaCl on drying shrinkage behavior of low-plasticity soil in earthen heritages. *Can Geotech J* 54:1762–1774. <https://doi.org/10.1139/cgj-2016-0403>
- Zhang Y, Ye WM, Chen B, Chen YG, Ye B (2016) Desiccation of NaCl-contaminated soil of earthen heritages in the Site of Yar City, northwest China. *Appl Clay Sci* 124–125:1–10. <https://doi.org/10.1016/j.clay.2016.01.047>
- Zhang Z, Yang Z, Wang S, Zhang L (2010) Weathering rates of a sandstone structure in a semi arid environment: a case study of the ancient city of Pingyao (world cultural heritage), China. *Bull Eng Geol Env* 70:231–237. <https://doi.org/10.1007/s10064-010-0316-9>
- Zhou L, Zhou F, Ying S, Li S (2021) Study on water and salt migration and deformation properties of unsaturated saline soil under a temperature gradient considering salt adsorption: Numerical simulation and experimental verification. *Comput Geotech* 134:104094. <https://doi.org/10.1016/j.compgeo.2021.104094>

Springer Nature or its licensor holds exclusive rights to this article under a publishing agreement with the author(s) or other rightsholder(s); author self-archiving of the accepted manuscript version of this article is solely governed by the terms of such publishing agreement and applicable law.